

Enhancing Plasticity Models by means of Data-Driven Correction

Rubén Ibáñez · Emmanuelle
Abisset-Chavanne · Elias Cueto ·
Francisco Chinesta · Antonio Huerta

Received: date / Accepted: date

Abstract To be filled.

Keywords: Data-Driven, Plasticity, Calibration.

1 Introduction

Plenty of effort has been dedicated throughout history to create very accurate models, as an example the reader may think about all different models formulated, for instance, in hyperelasticity like Neo-Hookean, Ogden, Saint-Venant. Another framework in which there are plenty of constitutive models is the one related to plasticity where we can highlight Tresca, Von Mises or Hill criteria among others. However, we also know that no model is perfect, it is always subjected to certain hypothesis. Indeed, even if you can calibrate a model perfectly well, no guarantee is given that for another set of experiences

R. Ibáñez & E. Abisset-Chavanne

ICI - High Performance Computing Institute, Ecole Centrale de Nantes

1 rue de la Noe, F-44300 Nantes, France

E-mail: Ruben.Ibanez-Pinillo@eleves.ec-nantes.fr

E-mail: Emmanuelle.Abisset-Chavanne@ec-nantes.fr

E. Cueto

Mechanical Engineering, Campus Rio Ebro, Zaragoza University

Maria de la Luna s/n, E-50018 Zaragoza, Spain

E-mail: ecuetos@unizar.es

A. Huerta

Laboratori de Càlcul Numèric, Universitat Politècnica de Catalunya

Jordi Girona 1-3, E-08034 Barcelona, Spain

E-mail: antonio.huerta@upc.edu

F. Chinesta *

PIMM - Procédés et Ingénierie en Mécanique et Matériaux, Ensam Paristech

151 boulevard de l'Hôpital, 75013 Paris, France

E-mail: Francisco.Chinesta@ensam.eu

* Corresponding author Francisco Chinesta

different from the calibration ones, the model is going to provide you a perfect result.

The main aim of this work is to provide an alternative route to enhance existing models including information coming from data, the so called data-driven correction. Particularly, special effort is placed into the calibration of plastic yield functions.

The data driven correction is quite simple, imagine that our departure point is a given model $\mathcal{M}(\mathbf{p})$. It is important to keep in mind that we are looking for a enhancement of the previous model, therefore a divergence model $\mathcal{D}(\mathbf{c})$, which applies to the first model, has to be defined. Therefore, reality (\mathcal{R}) is tried to be approximated as shown in eq. (1).

$$\mathcal{R} \approx \mathcal{M}(\mathbf{p}) + \mathcal{D}(\mathbf{c})|_{\mathbf{p}} \quad (1)$$

If we want to be truly objective, since our measurement capabilities will be constraint to some observable quantities, everything will depend from the set of experiences or observable quantities \mathcal{S} , as shown in eq. (2).

$$\mathcal{R}|_{\mathcal{S}} \approx \mathcal{M}(\mathbf{p}) + \mathcal{D}(\mathbf{c})|_{\mathbf{p}, \mathcal{S}} \quad (2)$$

It is worth to mention also that the way we define the observables \mathcal{S} could have an important impact over the calibration of the set of parameters, \mathbf{c} . Ideally, a set of experiences such that the entire parametric space \mathbf{c} is not singular has to be defined. Otherwise, it may lead to spurious modes in such parametric space.

2 Problem Statement

In the present work, we will try to capture the plastic yield function behind a given experiment. Just as a recall, a plastic yield function is a hypersurface living in the stress ($\boldsymbol{\sigma}$) space. Typically, this surface is parameterized using a finite set of parameters (\mathbf{p}) given by the first order model ($\mathcal{M}(\mathbf{p})$). Moreover, it will depend also on the correction model ($\mathcal{D}(\mathbf{c})$), therefore, a general plastic yield function can be written as shown in eq. (3).

$$\mathcal{F}_Y(\boldsymbol{\sigma}; \mathbf{p}, \mathbf{c}) = 0 \quad (3)$$

For the sake of simplicity, but without losing generality, we will constraint our set of experiences to plane stress hypothesis. Therefore, our plastic yield function is defined in a three dimensional space corresponding to the three active stress components ($\sigma_{xx}, \sigma_{yy}, \tau_{xy}$). Moreover, it is relatively easy to express it in spherical coordinates as shown in eqs. (4), since the plastic yield function is normally a convex closed surface.

$$\begin{aligned} \sigma_{xx} &= R \cos(\alpha) \sin(\beta) \\ \sigma_{yy} &= R \sin(\alpha) \sin(\beta) \\ \tau_{xy} &= R \cos(\beta) \end{aligned} \quad (4)$$

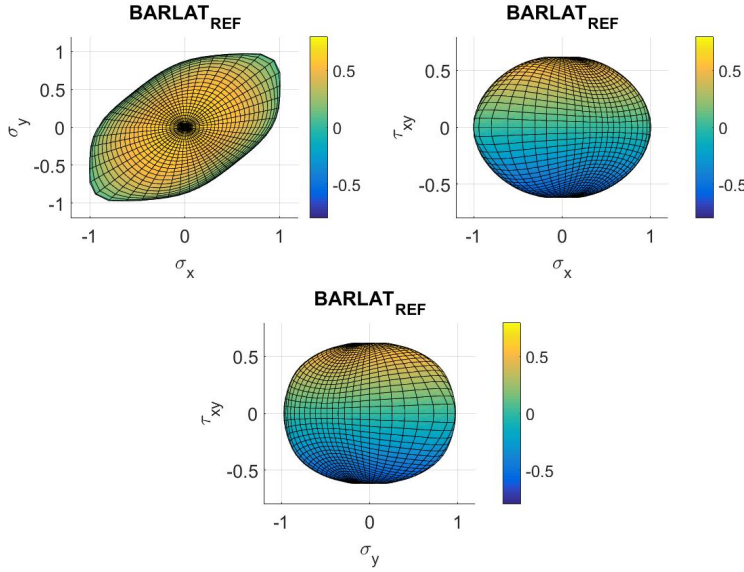


Fig. 1 Different views of Barlat Yld2004-18p plastic yield function. Colours are τ_{xy} .

Where $R(\alpha, \beta)$ function defines the radius in spherical coordinates for any possible angle. Therefore, a parameterization of $R(\alpha, \beta; \mathbf{p})$ directly determines the shape of \mathcal{F}_Y .

In a first step, we will work with synthetic data, since the main objective is to show the potential of the algorithm. Thus, reality (\mathcal{R}) is modeled using a Barlat Yld2004-18p yield function as shown in fig. (1).

The first model (\mathcal{M}) involves a quadratic Hill plastic yield function as shown in eq. (2). As it can be seen, this yield criterion presents a parameterization based on four coefficients, i.e. ($\#\mathbf{p} = 4$).

$$\mathcal{F}_Y^H(\sigma_{xx}, \sigma_{yy}, \tau_{xy}; F, G, H, N) = F\sigma_{yy}^2 + G\sigma_{xx}^2 + H(\sigma_{xx} - \sigma_{yy})^2 + N\tau_{xy}^2 - \sigma_0^2 \quad (5)$$

Fig. (2) depicts the shape of a quadratic Hill yield criterion when $F = 2.1$, $G = 1.8$, $H = 0.7$, $N = 1.9$. As it can be seen, convexity is fulfilled and it defines a smooth closed surface in the stress space.

The divergence model ($\mathcal{D}(\mathbf{c})$) involves a correction of the first model. This correction is done involving a set of 8 control points distributed along the plane $\tau_{xy} = 0$, plus another degree of freedom which relates to the movement of the maximum shear points defined in the line $(\sigma_{xx} = 0, \sigma_{yy} = 0)$, hence ($\#\mathbf{c} = 9$). The connexion between all degrees of freedom is done by means of a C1 continuous shape functions, also known as natural interpolation. Fig. (3) portrays the impact of moving one degree of freedom in $\mathcal{D}(\mathbf{c})$ on the quadratic Hill yield function depicted in fig. (2). As it can be seen, the maximum of the perturbation is achieved where the degree of freedom is placed and the magnitude is smoothly decreasing being minimum when the neighbouring degrees of freedom are reached.

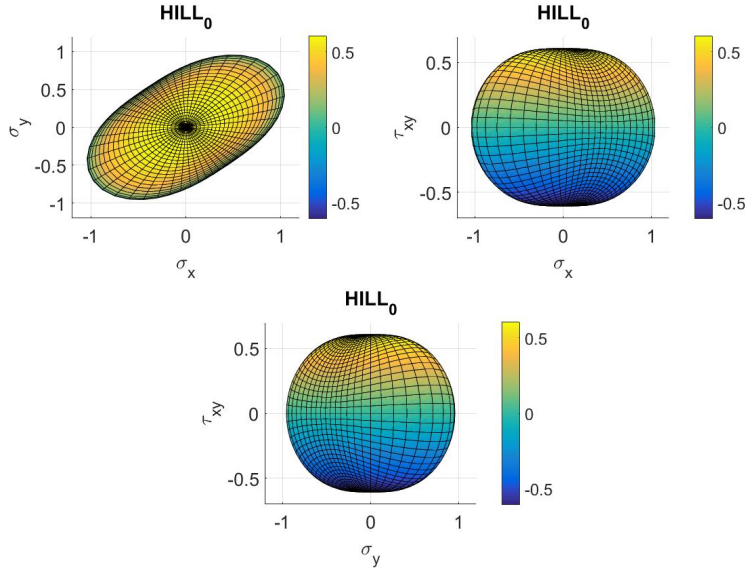


Fig. 2 Different views of quadratic Hill plastic yield function. Colours are τ_{xy} . $F = 2.1$, $G = 1.8$, $H = 0.7$ $N = 1.9$.

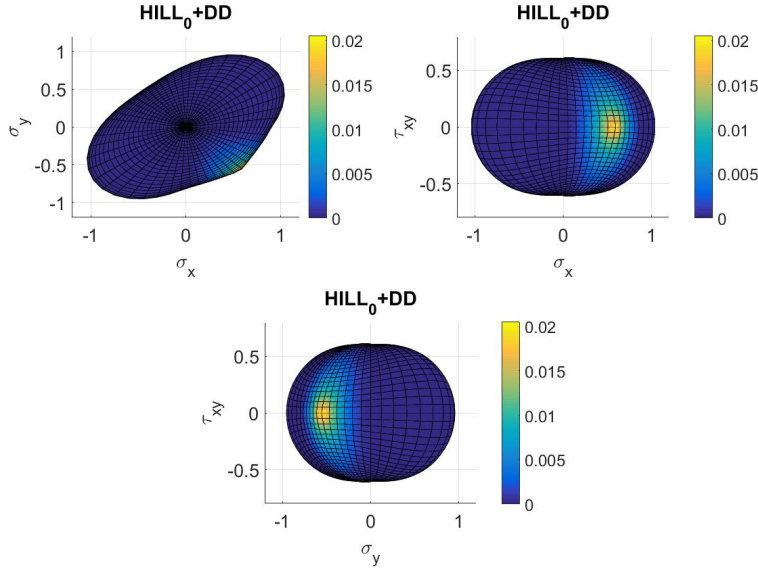


Fig. 3 Perturbed quadratic Hill plastic yield function moving only one dof of $\mathcal{D}(\mathbf{c})$. Colours are the magnitude of the perturbation. $F = 2.1$, $G = 1.8$, $H = 0.7$ $N = 1.9$.

Eq. (6) provides an error indicator which is able to quantify the discrepancies between the results simulating the set of experiences \mathcal{S} and the results provided by the real experiment. In this particular case, we select to measure the error using the strain field, but we could have done with the displacement field as well. If the first order model is already calibrated, the only parametric space that could vary is the one related to the divergence model.

$$E_{\mathcal{S}}(\mathbf{c}) = \sum_{s=1}^{\#\mathcal{S}} \int_{t_s} \int_{\mathbf{x}_s} \|\epsilon_{sim}^s(\mathbf{x}, t, \mathbf{c}) - \epsilon_{ref}^s(\mathbf{x}, t)\| d\mathbf{x} dt \quad (6)$$

The main idea is to build a response surfaces ($E_{\mathcal{S}}(\mathbf{c})$) to characterize the parametric spaces based on a existing set of experiences. Once the response surface is built, the global minimum of the response surface is going to provide the best candidate in the parametric space which is able to reproduce the set of experiences. Moreover, it is important to recall that our reality (\mathcal{R}) comes from a simulation using a Barlat Yld2004-18p, therefore we can always measure the error in the reconstructed plastic yield surface as shown in eq. (7).

$$E_{\mathcal{F}_Y}(\mathbf{c}) = \int_{\alpha} \int_{\beta} \|R_{ref}(\alpha, \beta) - R_{sim}(\alpha, \beta; \mathbf{c})\| d\alpha d\beta \quad (7)$$

Indeed, a perfect set of experiences will be the one providing a monotonic ratio between $E_{\mathcal{F}_Y}(\mathbf{c})$ and $E_{\mathcal{S}}(\mathbf{c})$, ensuring that the minimum in the strain error measure corresponds with the minimum in the plastic yield error measure. Otherwise, it will mean that our set of experiences may not be sensitive to certain variations in the parametric space.

3 Numerical Results

Two different set of quadratic Hill criterions have been used as a starting point in our perturbation model, \mathcal{H}_1 and \mathcal{H}_2 . The first one is already quite close to the Barlat's criterion, since it has a error $E_{\mathcal{F}_Y}^{\mathcal{H}_1} = 1.57$, whereas the second one presents an error of $E_{\mathcal{F}_Y}^{\mathcal{H}_2} = 24.9$. The parameter space to create both functions are $F_1 = 2.1$, $G_1 = 1.8$, $H_1 = 0.7$, $N_1 = 1.9$ and $F_2 = 2.3$, $G_2 = 2.0$, $H_2 = 0.8$, $N_2 = 1.7$, respectively. Fig. (4) portraits the error between the \mathcal{H}_1 criterion and the Barlat Yld2004-18p projected in the \mathcal{H}_1 criterion plastic surface.

Regarding the set of experiences (\mathcal{S}) to calibrate the models, we have chosen to use a set of relatively simple tests in a squared domain, $\Omega = [0, 1] \times [0, 1]$. The set of boundary conditions is specified in eqs. (8). Hence, varying the both tractions \mathbf{t}_1 and \mathbf{t}_2 , different regions of the stress space inside the piece of solid are explored. Indeed, 40 different experiments have been included in order to create $E_{\mathcal{S}}(\mathbf{c})$.

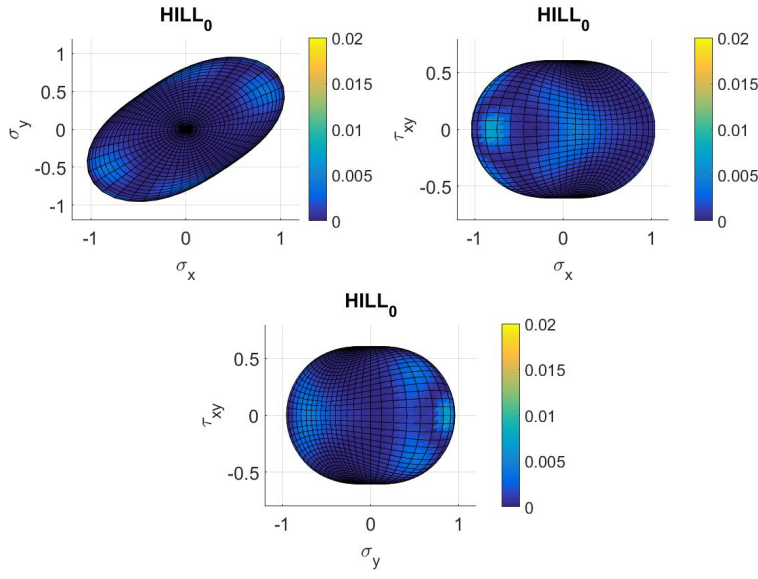


Fig. 4 Different views of \mathcal{H}_1 plastic yield function. Colours are mismatch between the \mathcal{H}_1 criterion and the Barlat Yld2004-18p. $E_{\mathcal{F}_Y}^{\mathcal{H}_1} = 1.57$.

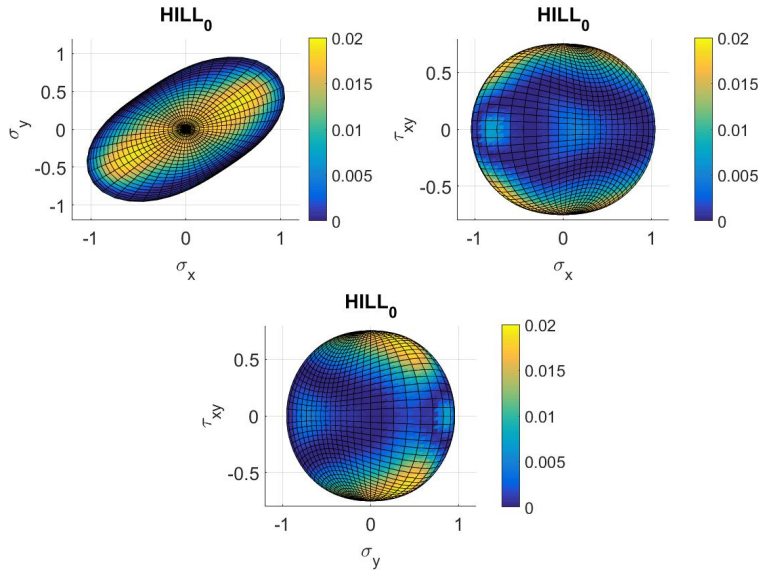


Fig. 5 Different views of \mathcal{H}_2 plastic yield function. Colours are mismatch between the \mathcal{H}_2 criterion and the Barlat Yld2004-18p. $E_{\mathcal{F}_Y}^{\mathcal{H}_2} = 24.9$.

$$\begin{aligned}
u(0, y) &= 0 \\
v(x, 0) &= 0 \\
\mathbf{t}(1, y) &= \mathbf{t}_1 \\
\mathbf{t}(x, 1) &= \mathbf{t}_2
\end{aligned} \tag{8}$$

In order to build the response surfaces $E_S^{\mathcal{H}_1}(\mathbf{c})$ and $E_S^{\mathcal{H}_2}(\mathbf{c})$, 1000 simulations, randomly selecting the parametric space, have been done for each case. Each realization of the parametric space follows a uniform distribution from $[-0.1, 0.1]$ in the \mathcal{H}_1 case and $[-0.15, 0.15]$ in the \mathcal{H}_2 case since we expect a major correction.

Several options could be adopted to reconstruct the entire response surface. Though non-structured interpolation techniques based on Delaunay triangulation can be used, they will suffer when the dimensionality of the parametric space increases. In this particular case, a non-linear regression technique called Sparse Proper Generalized Decomposition is used. It strongly relies on the separation of variables to circumvent the problem of high dimensional spaces, just like in a collocation method to build relatively smooth solutions from the available dataset. Indeed the main objective is to try to capture the whole response surface using less points. By doing that, instead of solving the direct problem plenty of times, we could have the possibility of inferring the minimum of the response surface using less points. Therefore, the sPGD algorithm is applied to half of the points previously precomputed in $E_S^{\mathcal{H}_2+DD}(\mathbf{c})$. The other half of the points are used to quantify the error in the prediction of the surface.

As it can be seen in Fig. (6) the response surface presents 7 percent of mean relative error. This error could be decreased easily if more sample points are added to the sPGD algorithm.

Once the response surface has a continuous and separated representation, the minimum is searched by employing a line search in each one of the separated directions. The initial point at which the line search algorithm is started is changed randomly to ensure the globality of the minimum.

Fig. (7) shows the error when the yield surface \mathcal{H}_1 is corrected with the data driven correction. As it can be seen, the final reconstructed error $E_{\mathcal{F}_Y}^{\mathcal{H}_1+DD}$, has been reduced with respect to the $E_{\mathcal{F}_Y}^{\mathcal{H}_1}$ error, passing from 1.57 to 1.27. Indeed, a 19 per cent of improvement has been achieved with the data driven correction for this particular case.

Fig. (8) shows the error when the yield surface \mathcal{H}_2 is corrected with the data driven correction. In this particular case, the final reconstructed error $E_{\mathcal{F}_Y}^{\mathcal{H}_2+DD}$ has been reduced as well from 24.9 to 4.63. Therefore, a 81 per cent of improvement has been produced in this particular case.

Finally, we have done a final simulation of a bar with the two right and left extremes campled in which a uniform vertical negative distributed load in both bottom and top sides of the bar is acting. The magnitude of the displacement field is shown in Fig. (9)

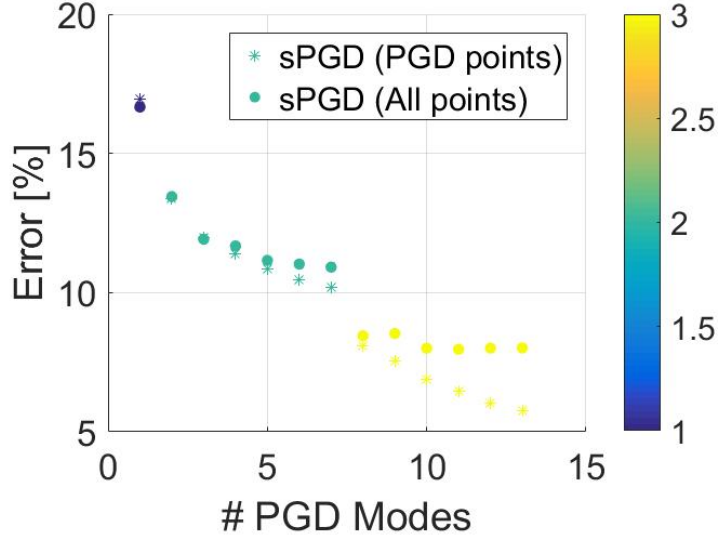


Fig. 6 Error in the reconstruction $E_S^{\mathcal{H}_2+DD}(\mathbf{c})$ using half of the points in the data base for training.

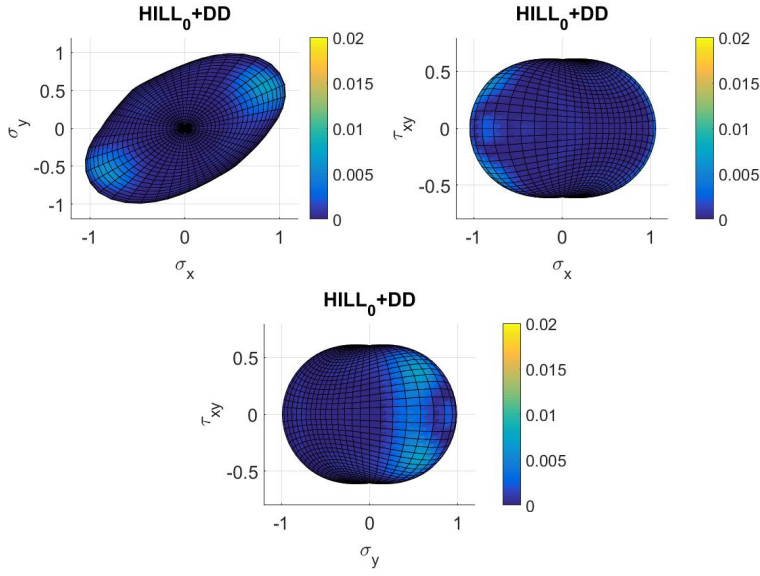


Fig. 7 Different views of $\mathcal{H}_1 + DD$ plastic yield function. Colours are mismatch between the $\mathcal{H}_1 + DD$ criterion and the Barlat Yld2004-18p. $E_{\mathcal{F}_Y}^{\mathcal{H}_1+DD} = 1.27$.

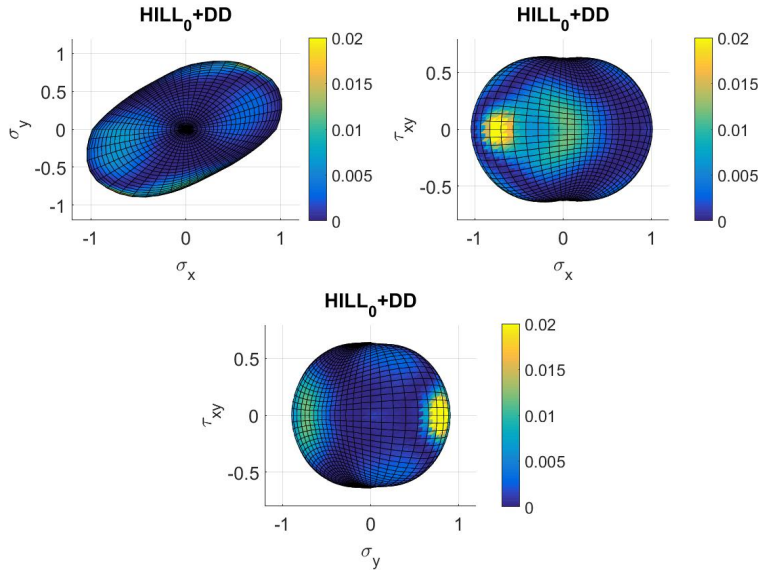


Fig. 8 Different views of $\mathcal{H}_2 + DD$ plastic yield function. Colours are mismatch between the $\mathcal{H}_2 + DD$ criterion and the Barlat Yld2004-18p. $E_{\mathcal{F}_Y}^{\mathcal{H}_2+DD} = 4.63$.

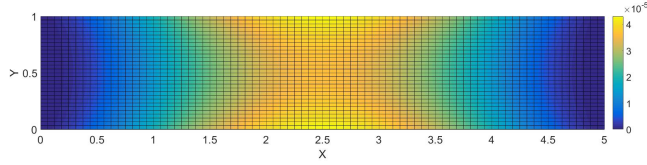


Fig. 9 Magnitude of displacement field under a bar with the two right and left extremes sampled in which a uniform vertical negative distributed load in both bottom and top sides of the bar is acting.

Fig. (10) shows the cumulated strain error between Barlat's and Hill's yield functions in the top. Bottom figure shows the error between Barlat's and Hill's plus data driven correction yield functions. As it can be seen, the error in the strain field is reduced when considering the correction. However, this error does not go to zero since the correction does not reproduce perfectly well Barlat's criterion.

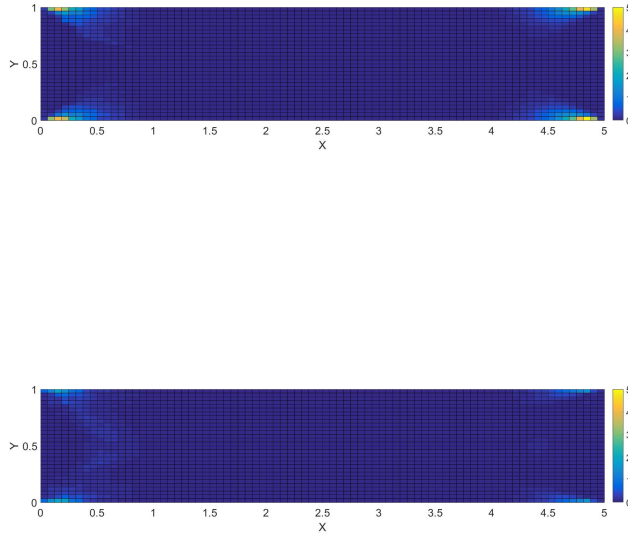


Fig. 10 Cumulated strain error between Barlat's and Hill in top and between Barlat's and Hill plus data correction in bottom.

In the light of the results, data driven correction importance is higher when the model is less accurate since the very beginning. In order to circumvent the problem of estimating a function in the high dimensional space, it is important to make use of smart interpolation techniques, which are able to provide us a reasonable estimation of the response surface.

4 Multi-PGD

A problem of the sPGD is that it may lead to a high number of modes when dealing with high dimensions. A way of circumventing this problem is to partition the domain using a coarse mesh and performing a low rank approximation (PGD) in each shape function related to the coarse mesh.

Imagine that the reference function shown in Fig. (11) is desired to be approximated in a low rank format for instance using a POD.

Fig. (12) shows the error in the solution when the field appearing in (11) is reconstructed using n POD modes.

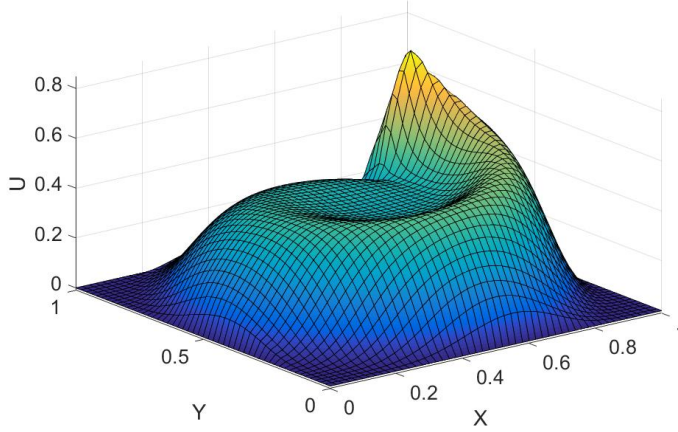


Fig. 11 A reference function.

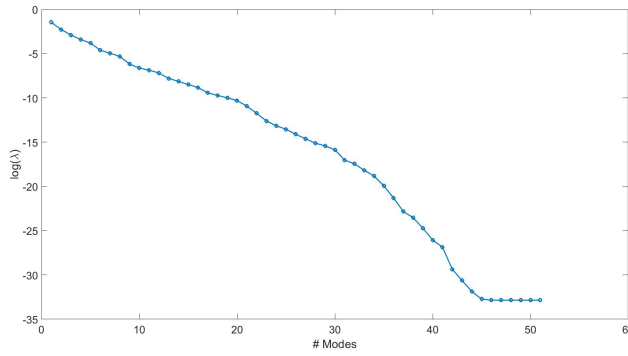


Fig. 12 Mean relative error of the approximation using n POD modes in logarithmic scale.

Fig. (13) shows how the multi-PGD approximation is done. Each red point relates to a local PGD approximation. The colour of each square is the number of PGD approximations that coexist in the element. Indeed, the number of PGD coexisting in the domain is 16.

Fig. (14) shows the reconstructed solution when only 1 PGD mode per subdomain is considered. If we reconstruct the error, we will achieve $1e-4$ in logarithmic scale, which is smaller than the solution provided by one global POD mode. Indeed to achieve such error we would need 4-5 global POD modes. Of course, since we have 16 PGDs acting in the domain, the solution will involve 16 local modes. Each PGD mode was discretized using 10 finite elements needing 352 entries to store the reference solution with a relative error of $1e-4$. Doing the same calculation for the global POD modes, each direction is dis-

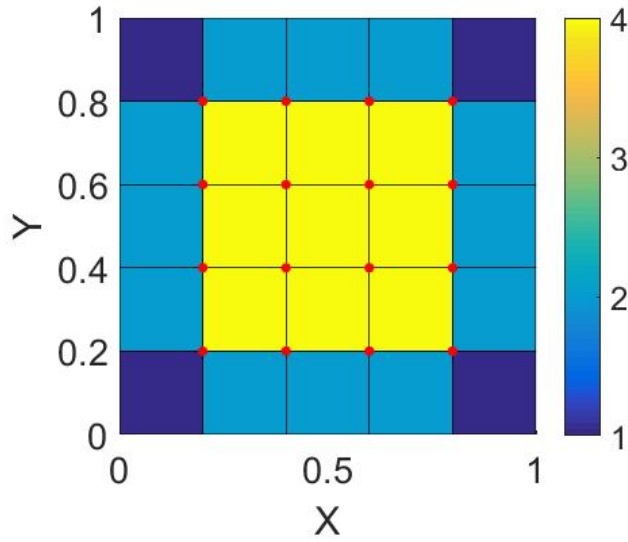


Fig. 13 Map of local PGD along the domain.

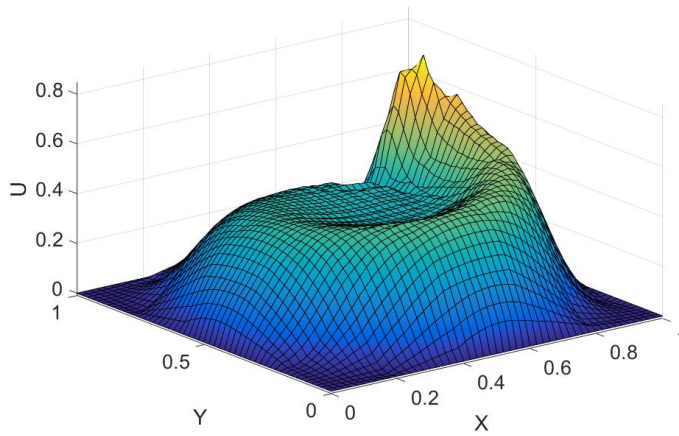


Fig. 14 Reconstruction of the solution using 1 PGD mode per subdomain.

cretized in 50 finite elements therefore using 5 global modes leads to 510 to store a solution with the same relative error than the local PGD. Therefore, this local separated representation may open the path to new compression techniques as well.